

**The future intensification of North Atlantic winter storm tracks: the key role  
of dynamic ocean coupling**

Rei Chemke\*

*Department of Earth and Planetary Sciences, Weizmann Institute of Science, Rehovot, Israel*

Laure Zanna

*Courant Institute of Mathematical Sciences, New York University, New York, NY, USA*

Clara Orbe

*NASA Goddard Institute for Space Studies, New York, NY, USA*

Lori T. Sentman

*NOAA/Geophysical Fluid Dynamics Laboratory, Princeton, New Jersey, USA*

Lorenzo M. Polvani

*Department of Applied Physics and Applied Mathematics, Department of Earth and  
Environmental Sciences, and Lamont-Doherty Earth Observatory, Columbia University, New  
York, NY, USA*

\*Corresponding author: Rei Chemke, rei.chemke@weizmann.ac.il

## ABSTRACT

Climate models project an intensification of wintertime North Atlantic storm tracks, over their downstream region, by the end of this century. Previous studies have suggested that ocean-atmosphere coupling plays a key role in this intensification, but the precise role of the different components of the coupling has not been explored and quantified. In this paper, using a hierarchy of ocean **coupling experiments**, we isolate and quantify the respective roles of thermodynamic (changes in surface heat fluxes) and dynamic ocean coupling (changes in ocean heat flux convergence) in the projected intensification of North Atlantic **transient eddy kinetic energy (TEKE)**. We show that dynamic coupling accounts for nearly all of the future **TEKE** strengthening as it overcomes the much smaller effect of surface heat flux changes to weaken the **TEKE**. We further show that by reducing the Arctic amplification in the North Atlantic, ocean heat flux convergence increases the meridional temperature gradient aloft, causing a larger eddy growth rate, and resulting in the strengthening of North Atlantic **TEKE**. Our results stress the importance of better monitoring and investigating the changes in ocean heat transport, for improving climate change adaptation strategies.

### **Plain-language significance statement**

By the end of this century North Atlantic storm tracks are projected to intensify on their eastward flank. Such intensification will have large societal impacts, mostly over western Europe. Thus, it is critical to better understand the mechanism underlying the intensification of the storm tracks. Here we investigate the role of ocean coupling in the future intensification of North Atlantic storm tracks, and find that ocean heat transport processes are responsible for the strengthening of the storm tracks. Our results suggest that better monitoring the changes in ocean heat transport will hopefully improve climate change adaption strategies.

## 38 1. Introduction

39 Mid-latitude storms play a central role in the weather and climate of the extra-tropics. These  
40 storms not only modulate the temperature, precipitation and winds over synoptic timescales, but  
41 also account for most of the energy (i.e., heat, moisture and momentum) transport from low to high  
42 latitudes, and across longitudes, over multi-decadal timescales. It is thus important to investigate  
43 the **mechanisms** associated with the mid-latitude storms' response to anthropogenic emissions.

44 In the Southern Hemisphere, climate models project a poleward shift of mid-latitude summer  
45 storm tracks, and an intensification of winter storm tracks. In the Northern Hemisphere, summer  
46 storm tracks are projected to weaken by the end of this century, while winter storm tracks to  
47 strengthen, mostly over the downstream region of the North Atlantic storm tracks (Chang et al.  
48 2012; Zappa et al. 2013; Harvey et al. 2014; Lehmann et al. 2014; Harvey et al. 2020). This eastward  
49 extension of North Atlantic storm tracks has great societal impacts, especially over western Europe  
50 (Zappa et al. 2013). **It should be noted that previous studies have found different magnitudes of**  
51 **the future North Atlantic storm tracks intensification, likely due to the different metrics used**  
52 **to define the storm tracks. For example, while a robust strengthening of the storm tracks**  
53 **was found using Eulerian metrics such as eddy variances (mostly at upper levels; Chang**  
54 **et al. 2012; Coumou et al. 2015) and sea level pressure (Harvey et al. 2014, 2020), a weaker**  
55 **strengthening of North Atlantic storm tracks was found using cyclone tracking algorithms**  
56 **(Zappa et al. 2013).**

57 Previous studies argued for the importance of ocean-atmosphere coupling in modulating North  
58 Atlantic winter storm tracks (Magnusdottir et al. 2004; Brayshaw et al. 2011). For example, the  
59 future changes, by the end of the 21st century, in winter sea surface temperature (SST) were  
60 argued to account for most of the intensification of North Atlantic storm tracks (Ciasto et al. 2016)

61 (whether this is a remote or local effect of the SST is still under debate, Ciasto et al. 2016;  
62 Gervais et al. 2019). In particular, the effects of **ocean dynamical changes** (i.e., the effects of  
63 ocean heat transport/uptake) were suggested to affect both the variability of North Atlantic storm  
64 tracks, and their projected response to anthropogenic emissions. For example, variations in the  
65 Atlantic Meridional Overturning Circulation (AMOC) and North Atlantic gyres were argued to  
66 modify the variability of North Atlantic storm tracks, via changes in SST (Frankignoul et al. 2013;  
67 Gastineau et al. 2013). In response to anthropogenic emissions, the AMOC was argued, based on  
68 a regression analysis, to modulate the intensification of North Atlantic winter storm tracks across  
69 the phase 3 of the Coupled Model Intercomparison Project (CMIP3) (Woollings et al. 2012), **and**  
70 **similarly, to modulate the jet's position across CMIP5 and CMIP6 models (Bellomo et al.**  
71 **2021).**

72 To further investigate the role of ocean heat transport changes in the North Atlantic storm  
73 tracks' response to anthropogenic emission, Woollings et al. (2012) used fixed ocean-heat-transport  
74 experiments: **the projected storm tracks' response by 2100 under the 20C3M and SRESA1B**  
75 **forcing scenarios, using fully-coupled models with active ocean heat transport, was compared**  
76 **to the storm tracks' response to doubling of CO<sub>2</sub> concentrations, using slab ocean models with**  
77 **fixed ocean heat transport.** Changes in ocean heat transport were mostly argued to contribute  
78 to the southward shift of the downstream region of North Atlantic storm tracks, but not to the  
79 intensification of the storm tracks. **Woollings et al. (2012), therefore, suggested that role of the**  
80 **AMOC in the storm tracks' response is overcome by other ocean heat transport processes.**

81 The use of different forcings (**future transient scenarios vs. equilibrated  $2 \times \text{CO}_2$  concentra-**  
82 **tions**) in the above experiments might have prevented Woollings et al. (2012) from fully quantifying  
83 the role of ocean heat transport changes in the storm tracks' response to anthropogenic emissions;  
84 **the different storm tracks response in the fully-coupled and fixed ocean-heat-transport ex-**

85 **periments might not only stem from the presence/absence of ocean heat transport changes**  
86 **but from the use of the different forcings as well (Supplementary Fig. 1).** Thus, the aim of this  
87 study is to quantify the role of ocean coupling, and in particular of ocean heat transport/uptake, in  
88 the intensification of North Atlantic winter storm tracks by the end of this century (**note that here**  
89 **we focus on the large-scale atmospheric response, and not on the interaction of individual**  
90 **storms with the ocean, Czaja et al. 2019).** Not only do we quantify the role of ocean coupling  
91 in the storm tracks' intensification, but we also elucidate the mechanism underlying the effect of  
92 ocean coupling on North Atlantic storm tracks. To accomplish this we build on previous fixed-  
93 ocean-coupling studies (Deser et al. 2016; Chemke and Polvani 2018; Chemke et al. 2019), and  
94 construct a hierarchy of **ocean coupling experiments** in large ensembles of model simulations  
95 forced by 20th and 21st century forcings.

## 96 **2. Methods**

### 97 *a. North Atlantic transient eddy kinetic energy*

98 Following previous studies (O’Gorman and Schneider 2008; Chang et al. 2012; Coumou et al.  
99 2015; Chemke and Ming 2020) we estimate the intensity of North Atlantic winter storm tracks  
100 through use of the December-February (DJF) vertically integrated transient eddy kinetic energy  
101 (TEKE),  $TEKE = \frac{1}{g} \int_0^{p_s} \left( \overline{u'^2} + \overline{v'^2} \right) dp$ , where  $g$  is gravity,  $p_s$  is surface pressure,  $p$  is pressure,  $u$  and  
102  $v$  are the zonal and meridional winds, respectively, and prime denotes deviation from monthly mean  
103 (denoted by overbar). **We here define the eddies as deviations from monthly mean since only**  
104 **monthly data of kinetic energy is available from the hierarchy of ocean coupling experiments**  
105 **used in this study. Nevertheless, the intensification of North Atlantic winter storm tracks**  
106 **found using a high bandpass filter (e.g., 2-6 days) in previous studies (see also Supplementary**

**Fig. 2)** is also clearly evident using deviations from monthly mean, as shown below. In addition, we define the downstream region of the storm tracks over the region,  $60^{\circ}\text{W} - 30^{\circ}\text{E}$  and  $40^{\circ}\text{N} - 60^{\circ}\text{N}$ , where most of the strengthening of the storm tracks occurs by the end of the 21st century (green boxes in Figs. 3a and 4a).

#### *b. CMIP5 models*

We analyze daily output of zonal and meridional winds from 14 CMIP5 models (Taylor et al. 2012) (BCC-CSM-1, BNU-ESM, CanESM2, CMCC-CMS, FGOALS-g2, FGOALS-s2, GFDL-CM3, GFDL-ESM2G, GFDL-ESM2M, IPSL-CM5A-LR, IPSL-CM5B-LR, MIROC-ESM, MIROC-ESM-CHEM, MPI-ESM-MR), **which were integrated between 1850 and 2100 under the Historical and Representative Concentration Pathway 8.5 (RCP8.5) forcings (Riahi et al. 2011).** We here use only the 'r1i1p1' realization in each model, in order to weigh all models equally.

#### *c. Hierarchy of ocean coupling experiments*

To quantify and elucidate the role of ocean coupling in the future North Atlantic TEKE changes by the end of this century we use the Community Earth System Model (**CESM1**) (Hurrell et al. 2013) and analyze a **hierarchy of ocean coupling experiments** in three large ensembles of model integrations. **The CESM1 comprises the Community Atmosphere Model (CAM V5.3), version 4 of the Los Alamos Sea Ice Model (CICE4), Los Alamos Parallel Ocean Program V2 (POP2), and Community Land Model V4.** Each ensemble includes a different ocean model component (full-physics or slab-ocean), and their combination elucidates the roles of different oceanic coupling processes in the North Atlantic TEKE response to anthropogenic emissions. Ocean coupling processes can be investigated via the mixed layer temperature equation, which

128 takes the simple form,  $\rho c_p h \frac{\partial T}{\partial t} = \text{SHF} + \text{OHFC}$ , where,  $\rho$  is sea-water density,  $c_p$  is the ocean  
129 specific heat capacity,  $h$  is the mixed layer depth,  $T$  is the **mixed-layer temperature**, SHF represents  
130 the net heat flux into the ocean from both atmosphere and sea-ice (surface heat fluxes), and OHFC  
131 is the ocean heat flux convergence in the mixed layer ( $\nabla \cdot (\mathbf{v}T)$ ; **including both horizontal and**  
132 **vertical heat fluxes**).

133 The first large ensemble (LE) is fully-coupled and described in Kay et al. (2015), and consists of  
134 40 members running from 1920-2100 under the same Historical and RCP8.5 forcings as in CMIP5.  
135 The first member of the ensemble is initialized from a long preindustrial control run, and at 1920  
136 all other members branch off the first member using a minor change in air temperature ( $O10^{-14}\text{K}$ ).  
137 Thus, the LE allows investigating the transient forced response of the system to external forcings,  
138 as the ensemble mean averages out the internal variability. Since the full-physics ocean model is  
139 used in LE, ocean coupling (i.e., ocean-atmosphere and ocean-sea-ice processes are active) can  
140 affect the TEKE response to external forcings over the 20th and 21st centuries.

141 The second ensemble consists of 20 members and has the same atmosphere, land and sea-ice  
142 model components as the LE but a different ocean component: the full-physics ocean model is  
143 replaced with a slab ocean model. **In the slab ocean model ensemble (SOM LE) the OHFC**  
144 **and mixed layer depth vary spatially, but are fixed to monthly and annual values, respectively**  
145 **(i.e., fixed dynamic coupling), calculated from the climatology of a long preindustrial control**  
146 **run using the fully-coupled model.** Thus, in SOM LE changes in ocean horizontal heat transport  
147 and vertical heat uptake **by the deep ocean (note that the mixed layer depth is also fixed as it**  
148 **accounts for part of the vertical heat mixing)** cannot affect the TEKE response to anthropogenic  
149 emissions. Comparing the response in LE and SOM LE isolates, and thus enables quantifying, the  
150 role of OHFC changes, including both horizontal heat transport and vertical heat uptake **by the**

151 **deep ocean (vertical heat transfer via diffusion/convection/advection) in the TEKE response.**  
152 **Note that the dynamic coupling component accounts for the impacts of OHFC and not only**  
153 **the impacts of the oceanic circulation.**

154 **A few clarifications on the SOM LE. First, the sea-ice component, i.e., the dynamic–**  
155 **thermodynamic sea-ice model, CICE4, may affect the mixed-layer temperature via latent**  
156 **and sensible heat fluxes associated with open-ocean snow fall and sea-ice growth, surface**  
157 **lateral and basal fluxes and ice runoff (Bitz et al. 2012). Second, since the OHFC and mixed**  
158 **layer depth in SOM LE are calculated from the mixed layer temperature equation in the**  
159 **preindustrial run of the fully coupled model, the two ensembles are initialized from a very**  
160 **similar background state (Fig. 1); the differences between the background states of the TEKE**  
161 **in the two simulations are statistically insignificant and of almost two order of magnitudes**  
162 **smaller than the TEKE climatology (Supplementary Fig. 3). Lastly, the SOM LE is constructed**  
163 **in the same way as LE: the first member is initialized from a long preindustrial control run of 900**  
164 **years, and all other members branch off the first member at 1920, and run from 1920-2099 (under**  
165 **the same forcings as in LE).**

166 **For consistency with the large body of work done on the role of SST in the climate’s response**  
167 **to increased greenhouse gases using atmosphere-only runs (e.g., Ciasto et al. 2016), the third**  
168 **ensemble is similar to SOM LE (consists of 20 members using the slab ocean model of CESM1**  
169 **forced under the Historical and RCP8.5 forcings) except for the mixed-layer temperature which**  
170 **is kept constant at preindustrial values. Thus, in this ensemble there is no active ocean model**  
171 **(NOM LE), as both OHFC and SHF cannot affect the TEKE response. Comparing the TEKE**  
172 **response in LE and NOM LE isolates the role of net ocean coupling over the 20th and 21st**  
173 **centuries. Note that the NOM LE runs are slightly different than atmosphere-only runs,**  
174 **where both SST and sea-ice are fixed, since in NOM LE only the SST is prescribed (here to**

175 preindustrial values). This allows isolating only the net role of ocean coupling, without the  
176 net role of sea-ice coupling, as sea-ice-atmosphere interactions can affect the TEKE response  
177 (the sea-ice is treated as in SOM LE).

178 Furthermore, comparing the TEKE response in SOM LE and NOM LE isolates the effect of  
179 SHF, as these processes are active in SOM LE but not in NOM LE. Following previous studies  
180 (e.g., Deser et al. 2016), we refer to the SHF (i.e., the impact of ocean-atmosphere and ocean-  
181 sea-ice heat fluxes on the mixed-layer temperature) as thermodynamic ocean coupling. Thus,  
182 by construction, the sum of the difference between LE and SOM LE and the difference between  
183 SOM LE and NOM LE yields the net effect of ocean feedbacks (i.e., the difference between  
184 LE and NOM LE); such decomposition allows one to investigate the different processes that  
185 modulate the SST response (i.e., the SHF and OHFC in the mixed-layer equation), as inferred  
186 from the fixed SST runs.

187 Finally, we verify that each ensemble is sufficiently large to capture the variability of North  
188 Atlantic TEKE over the downstream region of the storm tracks by calculating the TEKE variability  
189 (defined as one standard deviation of inter-member spread) across different number of ensemble  
190 members ( $n$ ). In particular, we calculate the standard deviation in each combination of  
191 ensemble members (or up to 1000 random combinations) of size  $n$ , and average over all  
192 combinations. This is done for each year over the 1920-2099 period, and the mean over all  
193 years is shown in Fig. 2. Fig. 2 shows that 12, 13 and 15 members in NOM LE, SOM LE and  
194 LE, respectively, already capture 99% (marked by the vertical lines) of the TEKE variability in  
195 the ensembles. Thus, the size of each ensemble is sufficiently large to capture the variability and  
196 forced response of North Atlantic TEKE.

197 *d. Ocean heat flux convergence experiments under idealized forcing*

198 To ensure that the role of OHFC in the TEKE response to anthropogenic emissions in **CESM1**  
199 **is robust and evident in other models**, we also analyze fixed-OHFC experiments in two other  
200 models: the NASA Goddard Institute for Space Studies Model E2.1 (GISS Model E2.1) (Kelley  
201 et al. 2020), and the Geophysical Fluid Dynamics Laboratory’s CM4.0 (GFDL CM4) (Held et al.  
202 2019). Similar to the ocean experiments in **CESM1**, we make use of the fully-coupled and slab  
203 ocean (with fixed OHFC and mixed layer depth, **and the same dynamic-thermodynamic sea-ice**  
204 **model as in the fully coupled** models) versions of the GISS Model E2.1 and GFDL CM4, only  
205 here forced by an abrupt quadrupling of CO<sub>2</sub> concentrations, relative to preindustrial values. This  
206 allows us to qualitatively verify the results from **CESM1**, as CO<sub>2</sub> concentrations, in the RCP8.5  
207 scenario, are expected to approximately quadruple by the end of this century. For the fully-coupled  
208 and slab ocean models in GISS Model E2.1 we use the last 40 years of 150-year and 60-year runs,  
209 respectively. In GFDL CM4, we use the last 40 years of 150-year run in both the slab ocean and  
210 fully-coupled models. **Note that corresponding NOM simulations are not available from these**  
211 **models.**

212 *e. Linear normal mode instability analysis*

213 To investigate the mechanism underlying the role of ocean coupling in the projected changes of  
214 North Atlantic TEKE, we follow previous studies (e.g., Smith 2007; Chemke and Polvani 2019;  
215 Chemke and Ming 2020) and apply a linear normal-mode instability analysis to the quasigeostrophic  
216 equations over the North Atlantic region in the hierarchy of **ocean coupling experiments**. This  
217 analysis allows us to examine the growth rate of North Atlantic storm tracks, which is a widely used  
218 metric for the baroclinicity of the flow, i.e., the extraction of energy, by the eddies, from the mean  
219 flow. The quasigeostrophic equations, linearized about a mean state, can be written as follows,

$$\begin{aligned}
\frac{\partial q'}{\partial t} + \bar{\mathbf{u}} \cdot \nabla q' + \mathbf{u}' \cdot \nabla \bar{q} &= 0, p_{\text{trop}} < p < p_s \\
\frac{\partial}{\partial t} \frac{\partial \psi'}{\partial p} + \bar{\mathbf{u}} \cdot \nabla \frac{\partial \psi'}{\partial p} + \mathbf{u}' \cdot \nabla \frac{\partial \bar{\psi}}{\partial p} &= 0, p = p_{\text{trop}}, p_s,
\end{aligned} \tag{1}$$

220 where the first equation is derived from the conservation of quasigeostrophic potential vorticity  
 221 ( $q$ ) at the interior, and the second from conservation of potential temperature ( $\theta$ ) at the surface  
 222 and tropopause height ( $p_{\text{trop}}$ ). The quasigeostrophic eddy potential vorticity can be written as,  
 223  $q' = \nabla^2 \psi' + \Gamma \psi'$ , where  $\psi = \phi/f$  is the streamfunction,  $\phi$  is the geopotential,  $f$  is the Coriolis  
 224 parameter,  $\Gamma = \frac{\partial}{\partial p} \frac{f^2}{S^2} \frac{\partial}{\partial p}$  is a second-order differential operator,  $S^2 = -\frac{1}{\rho \theta} \frac{\partial \theta}{\partial p}$  is static stability and  $\rho$   
 225 is density. The mean quasigeostrophic potential vorticity gradient is defined as  $\nabla \bar{q} = \Gamma \bar{v} \hat{i} + (\beta - \Gamma \bar{u}) \hat{j}$ ,  
 226 where  $\beta$  is the meridional derivative of  $f$  and  $\nabla \frac{\partial \bar{\psi}}{\partial p} = \frac{\partial \bar{v}}{\partial p} \hat{i} - \frac{\partial \bar{u}}{\partial p} \hat{j}$ . Transforming Eq. 1 to an eigenvalue  
 227 problem, using a plane-wave solution,  $\psi' = \text{Re} \{ \hat{\psi}'(p) e^{i(kx - \omega t)} \}$ , allows one to explore the growth  
 228 rate of the waves (**between  $p_s$  to  $p_{\text{trop}}$** ), which is represented by the imaginary component of  
 229 the frequency,  $\omega$  (the eigenvalue); we here analyze the fastest growth rate. The input for the  
 230 eigenvalue problem is the mean North Atlantic wintertime fields (i.e., temperature, zonal wind  
 231 and tropopause height) from each ensemble, averaged over the **downstream region of the storm**  
 232 **tracks (calculating the growth rate over the upstream region of the storm tracks, does not**  
 233 **allow the growth rate to capture the TEKE response over the downstream region).**

234 The linear normal mode instability analysis allows one to account for the vertical variations  
 235 in the zonal wind shear and static stability **changes**, which are usually overlooked when using a  
 236 more simplified metric of the growth rate, such as the Eady growth rate. These variations play an  
 237 important role in the effects of ocean coupling on the North Atlantic TEKE response (as shown  
 238 below). **Lastly, note that while the above analysis accounts for the effects of the mean flow on**  
 239 **the eddies, it does not account for the effects of the eddies on the mean flow.**

240 *f. Student's t-test*

241 For estimating the significance of the response of different fields to anthropogenic emissions  
242 (i.e., the difference between the 2080-2099 and 1980-1999 periods) we here use dependent t-  
243 test for paired samples in each ensemble; the number of degrees of freedom is defined as  
244  $n - 1$ , where  $n$  represents the number of ensemble members (pairs). The significance of the  
245 difference between the different ensembles is estimated via independent two-sample t-test.

246 **3. Results**

247 *a. Quantifying the role of ocean coupling in the projected response of North Atlantic TEKE to*  
248 *anthropogenic emissions*

249 We start by considering the response to anthropogenic emissions (difference between the last 20  
250 years of the 21st and 20th centuries) of DJF North Atlantic TEKE in the CMIP5 models (shading  
251 in Fig. 3a shows the response and black contours the TEKE climatology averaged over the last  
252 20 years of the 20th century). As noted in previous studies (Chang et al. 2012; Harvey et al.  
253 2014; Lehmann et al. 2014; Harvey et al. 2020), wintertime North Atlantic TEKE is projected  
254 to strengthen mostly over the downstream region of the storm tracks **and to a lesser extent**  
255 **over North-East America**, and to slightly weaken at higher and lower latitudes. In particular,  
256 averaging the TEKE response over the downstream region of the storm tracks (green rectangle  
257 in Fig. 3a, where most of the intensification occurs) yields a multi-model mean strengthening of  
258  $9.56 \times 10^4 \text{ Jm}^{-2}$  in TEKE (vertical black line in Fig. 3b). Note that two models, out of the 14  
259 models analyzed in this study, do not show any TEKE intensification over the downstream region  
260 of the storm tracks (gray bars in Fig. 3b). Nonetheless, the strengthening is clearly evident in the  
261 multi-model mean.

We next turn to isolate the role of ocean coupling in the intensification of wintertime North Atlantic TEKE using the **hierarchy of ocean coupling experiments** in CESM1. Before analyzing the CESM1 ensembles, we first ensure that the projected forced response in LE is not an outlier within the CMIP5 models. The LE mean response of wintertime North Atlantic TEKE over the downstream region of the storm tracks ( $1.05 \times 10^5 \text{ Jm}^{-2}$ , red line in Fig. 3b) is very similar to the CMIP5 mean response (compare red and black lines), and thus is well within the response of the CMIP5 ensemble. **This provides us confidence to use CESM1 for quantifying the role of ocean coupling in the future intensification of North Atlantic TEKE.**

The spatial pattern of the North Atlantic TEKE response to anthropogenic emissions in the LE mean and the relative contributions from the different ocean coupling components are shown in Fig. 4. First, as in the CMIP5 mean (Fig. 3a), the LE mean exhibits a strengthening of North Atlantic TEKE mostly over the downstream region of the storm tracks, with a reduction at lower and higher latitudes (shading in Fig. 4a shows the response and black contours the TEKE climatology averaged over the last 20 years of the 20th century). **Unlike in the CMIP5 mean, the LE mean does not show a strengthening over North-East America, and the weakening at high latitudes is more robust; these differences between the LE and CMIP5 might be artefacts of the CESM1 configuration. Nevertheless, the LE adequately simulates the strengthening of the TEKE over the downstream region of the storm tracks as in the CMIP5 models.** Second, isolating the role of ocean coupling in the TEKE response (i.e., taking the difference between LE and NOM LE, Fig. 4b) shows that ocean coupling accounts for most of the strengthening of North Atlantic TEKE over the downstream region of the storm tracks **(in the absence of ocean coupling, i.e., in the NOM LE simulations, changes in the atmosphere, land and sea-ice yield insignificant changes in TEKE, Supplementary Fig. 4a).** This verifies the findings of Ciasto et al. (2016), who argued

that the projected SST response by the end of the century accounts for most of the intensification of North Atlantic TEKE.

Given the important role of ocean coupling in the TEKE response we further decompose the ocean's contribution to thermodynamic coupling (i.e., the difference between SOM LE and NOM LE) and dynamic coupling (i.e., the difference between LE and SOM LE). While thermodynamic coupling (the effects of SHF) acts to weaken the North Atlantic TEKE by the end of this century (Fig. 4c), dynamic coupling (the effects of OHFC) acts to strengthen the TEKE (Fig. 4d). Thus, changes in OHFC are responsible for the intensification of North Atlantic TEKE; without changes in OHFC (i.e., in the SOM LE simulations) North Atlantic TEKE would have weakened by 2100 over the poleward and equatorward flanks of the storm tracks (Supplementary Fig. 4b).

Before further investigating the role of OHFC in the TEKE response, it is important to verify that the effect of OHFC to intensify the North Atlantic TEKE does not depend on the specific formulations of CESM1. We thus next analyze the TEKE response in the fully coupled and slab ocean configurations of two other models: GISS Model E2.1 and GFDL CM4 (Methods). In both models we analyze the TEKE response to an abrupt quadrupling of CO<sub>2</sub> concentrations, relative to preindustrial values. We choose the abrupt 4×CO<sub>2</sub> experiment, as it is expected to qualitatively yield similar results to the RCP8.5 experiment used in CESM1, where CO<sub>2</sub> levels are projected to approximately quadruple, relative to preindustrial values, by 2100.

First, similar to CESM1 and the CMIP5 mean (Figs. 4a and 3a), both GISS Model E2.1 (Fig. 5a) and GFDL CM4 (Fig. 5c) exhibit a strengthening of North Atlantic TEKE over the downstream region of the storm tracks under quadrupling of CO<sub>2</sub> concentrations (shading shows the response and black contours the TEKE preindustrial climatology). **The pattern of this strengthening, however, is slightly different in these two models. While, similar to CESM1 and the CMIP5 mean, the strengthening of the TEKE in GFDL CM4 is confined to the downstream region**

309 of the storm tracks, in GISS Model E2.1 the strengthening is evident throughout the North  
310 Atlantic region. This suggests that the different models' configurations might affect the  
311 distribution of the TEKE response. Nonetheless, the strengthening over the downstream  
312 region of the storm tracks is clearly evident in both models.

313 Second, the role of OHFC in strengthening the TEKE in these models (evaluated by taking  
314 the difference between the TEKE response in the fully coupled and slab ocean configurations) is  
315 similar to the one projected in CESM1: OHFC accounts for most of the strengthening of North  
316 Atlantic TEKE over the downstream region of the storm tracks (Fig. 5b and 5d). **Note that the role**  
317 **of OHFC in the TEKE response is larger in CESM1 in comparison to the GISS Model E2.1**  
318 **and GFDL CM4 models. One explanation for this difference is the use of different forcings**  
319 **to evaluate the OHFC role. Indeed, under an abrupt  $4 \times \text{CO}_2$  forcing, the role of OHFC in**  
320 **the TEKE response in CESM1 is similar to the OHFC role in the GISS Model E2.1 and**  
321 **GFDL CM4 models (Supplementary Fig. 5). Thus, the magnitude of the effect of OHFC to**  
322 **intensify the TEKE might vary across models and forcings. Nevertheless, the above analysis**  
323 **provides us confidence that the important role of changes in OHFC to drive the projected**  
324 **intensification of North Atlantic TEKE is robust, and is not an artifact of the CESM1.**

325 To quantify the roles of the different ocean coupling components in the TEKE response to  
326 anthropogenic emissions in CESM1 we next compare the averaged TEKE response over the  
327 downstream region of the storm tracks across the different ensembles (Fig. 6a). First we consider the  
328 effects of total oceanic coupling. The TEKE intensification due to ocean coupling ( $1.09 \times 10^5 \text{ Jm}^{-2}$ ,  
329 vertical black line) accounts for nearly all of the LE mean TEKE response ( $1.05 \times 10^5 \text{ Jm}^{-2}$ , vertical  
330 red line). Thus, without **ocean feedbacks** North Atlantic TEKE is not expected to strengthen over  
331 the downstream region of the storm tracks. Further decomposing the ocean's contribution to  
332 thermodynamic (SHF, green bars) and dynamic (OHFC, blue bars) coupling shows that while

changes in SHF act to weaken the North Atlantic TEKE by  $-2.55 \times 10^5 \text{ Jm}^{-2}$  (vertical green line), changes in OHFC act to intensify the TEKE by  $3.64 \times 10^5 \text{ Jm}^{-2}$  (vertical blue line). Thus, North Atlantic TEKE is projected to intensify by the end of the 21st century as the effect of SHF to weaken the TEKE is overcome by the large effect of OHFC to strengthen it.

**The effects of OHFC on North Atlantic TEKE can be separated into the effects of net oceanic heat uptake by the deep ocean (i.e., global mean mixed-layer OHFC) and of horizontal heat redistribution by ocean heat transport and non-uniform heat uptake (the difference between OHFC and net heat uptake).** To disentangle these two processes we next normalize the TEKE response by the global mean SST response. This normalization eliminates the role of net oceanic heat uptake by the deep ocean (i.e., global mean heat uptake) in delaying surface warming: the different global mean sea surface warming in LE and SOM LE is only due to changes in net oceanic heat uptake by the deep ocean. Thus, the difference in the normalized TEKE response in LE and SOM LE isolates the contribution from horizontal heat redistribution. Fig. 6b shows the TEKE response normalized by the global mean SST response in LE (red bars), along with the contribution from changes in horizontal heat redistribution (blue bars). Horizontal heat redistribution by ocean dynamics results in an intensification of  $8.4 \times 10^4 \text{ Jm}^{-2}\text{K}^{-1}$  (vertical blue line), which is 2.2 times larger than the intensification, scaled by the global mean SST response, in LE ( $3.8 \times 10^4 \text{ Jm}^{-2}\text{K}^{-1}$ , vertical red line). Since total OHFC results in an intensification that is 3.4 times larger than the projected TEKE intensification in LE (blue and red bars in Fig. 6a), changes in horizontal heat redistribution account for almost two thirds of the effect of ocean heat transport to intensify the North Atlantic TEKE; one third of the intensification is due to changes in net oceanic heat uptake by the deep ocean.

The result that the intensification of North Atlantic TEKE is mostly due to changes in horizontal heat redistribution is different than one reported in Woollings et al. (2012), where OHFC

was argued to shift the storm tracks southward, with little effect on their intensity (cf. Fig. 3i in Woollings et al. 2012). As discussed in Sec. 1, since the fully coupled and slab ocean models analyzed in Woollings et al. (2012) were forced by different forcings (the 20C3M and SRESA1B forcing scenarios vs. an idealized forcing of  $2 \times \text{CO}_2$ ), their comparison does not only isolate the role of ocean heat transport changes, but also the effects of the different external forcings used in these experiments (transient vs. equilibrated forcings, with different  $\text{CO}_2$  levels).

To further demonstrate the importance of using the same forcings across the different simulations in such an attribution analysis, we next investigate the role of OHFC in the projected TEKE intensification in LE using slab ocean model simulations under  $2 \times \text{CO}_2$  and  $4 \times \text{CO}_2$  forcings. First, as in Woollings et al. (2012), comparing the future TEKE response in LE to the response in the slab ocean model version of CESM1 under  $2 \times \text{CO}_2$  forcing suggests that OHFC acts to reduce the TEKE intensity on the poleward flank of the storm tracks and increase the TEKE intensity on the equatorward flank, thus acting to shift the TEKE southward (Supplementary Fig. 6a). Second, forcing the slab ocean model with an abrupt quadrupling of  $\text{CO}_2$  concentrations, shows that the effect of OHFC to shift the storm tracks equatorward is significantly reduced, as OHFC acts to intensify the TEKE over most of the low-mid latitudes, with minor changes on the poleward flank of the storm tracks (Supplementary Fig. 6b). Lastly, using the same forcings in both LE and the slab ocean model shows that OHFC does not contribute to the southward shift of the storms, but mostly intensifies the TEKE over the entire North Atlantic region (Fig. 4d and Supplementary Fig. 6c).

The above analysis emphasizes that in order to adequately capture the role of OHFC it is critical to use the same forcings across the hierarchy of ocean coupling experiments. It is important to use not only the same magnitude of forcings, but also the same transient

evolution of the forcing; the climate’s response to increased greenhouse gases was found to vary over different time scales (Grise and Polvani 2017; Ceppi et al. 2018). Lastly we note that another difference that might contributes to the different TEKE responses in the CMIP3 slab ocean models analyzed in Woollings et al. (2012) and the SOM LE analyzed here is the representation of dynamic sea-ice, which is active in SOM LE but not in all CMIP3 models (note that, as in SOM LE, thermodynamic sea-ice models were present in CMIP3 models).

*b. Elucidating the mechanism underlying the effects of ocean coupling on future North Atlantic TEKE*

Since winter mid-latitude storm tracks are driven by baroclinic instability, investigating the future changes in the baroclinicity of the flow can provide meaningful insights on the projected storm tracks’ response to anthropogenic emissions. In particular, we follow **previous** studies (e.g., Brayshaw et al. 2011; Frankignoul et al. 2013; Gastineau et al. 2013; Chemke and Polvani 2019; Chemke and Ming 2020) and investigate the fastest growth rate of the eddies, as a measure for baroclinicity. To calculate the growth rate of North Atlantic eddies we conduct a linear normal-mode instability analysis of the quasigeostrophic equations, linearized about the mean state of the downstream region of North Atlantic storm tracks (Methods). The analysis is conducted using the mean fields (zonal wind, static stability and tropopause height), averaged over the last 20 years of the 20th and 21st centuries, from each large ensemble.

First, in accordance with the intensification of North Atlantic TEKE by the end of this century, the growth rate of the waves in LE mean is also projected to increase ( $7.1 \times 10^{-7} \text{ s}^{-1}$ , red bar in Fig. 6c). Furthermore, ocean coupling **increases** the growth rate by  $7.4 \times 10^{-7} \text{ s}^{-1}$  (gray bar in Fig. 6c), which demonstrates that, as for the TEKE intensity, having an active ocean results in the future increase of the eddies’ growth rate. Second, decomposing the role of ocean coupling to

thermodynamic and dynamic coupling shows that while thermodynamic coupling (SHF) acts to reduce the growth rate by the end of this century ( $-4.8 \times 10^{-7} \text{ s}^{-1}$ , green bar in Fig. 6c), dynamic coupling (OHFC) is responsible for the future increase in the growth rate ( $1.2 \times 10^{-6} \text{ s}^{-1}$ , blue bar in Fig. 6c). Thus, changes in the growth rate due to the different oceanic components **are consistent with** the effects of these oceanic components on the TEKE response to anthropogenic emissions. **Note that the growth rate shows low correlation with the TEKE response across the different members in each ensemble, suggesting that the instability analysis might be insensitive to variations that arise from internal variability. Nevertheless, since here we focus on the role of ocean coupling in the forced response of TEKE,** the above analysis provides us the confidence to investigate the growth rate changes to better understand the role of ocean coupling in the TEKE response.

The advantage of simplifying the North Atlantic storm tracks behavior to an eigenvalue problem is that it allows one to isolate the role of the mean fields in the storm tracks' response to anthropogenic emissions. This is done by re-solving Eq. 1 for the last 20 years of the 21st century while keeping all mean fields at their last 20 years of the 20th century values **except** for one: the difference between the resulting growth rate and the growth rate of the last 20 years of the 20th century isolates the role of each mean field in the growth rate response to anthropogenic emissions. Fig. 6d shows the relative contributions of the mean zonal wind, static stability and tropopause height to the response of the growth rate of North Atlantic eddies across the different ensembles. First, the increase in the growth rate in LE (red bars) is due to changes in the zonal wind ( $7.4 \times 10^{-7} \text{ s}^{-1}$ ). Changes in static stability, on the other hand, act to decrease the growth rate in LE, and thus to oppose its projected increase ( $-1.5 \times 10^{-7} \text{ s}^{-1}$ ). Second, since ocean coupling (gray bars) is responsible for the increase in the growth rate (Fig. 6c), it also increases the growth rate via changes in the zonal wind ( $8.1 \times 10^{-7} \text{ s}^{-1}$ ), while its effect on static stability acts to decrease the growth rate

response ( $-1.9 \times 10^{-7} \text{ s}^{-1}$ ). Interestingly, while thermodynamic coupling (SHF, green bars) acts to reduce the growth rate response via changes in both zonal wind ( $-1.9 \times 10^{-7} \text{ s}^{-1}$ ) and static stability ( $-2.8 \times 10^{-7} \text{ s}^{-1}$ ), dynamic coupling (OHFC, blue bars) overcomes the SHF tendency and acts to increase the growth rate via changes in the zonal wind ( $1 \times 10^{-6} \text{ s}^{-1}$ ). The tropopause height has a minor contribution to the increase in the growth rate, mostly via OHFC changes.

To better understand the role of ocean coupling in the response of the growth rate of North Atlantic eddies we next analyze the response of the mean temperature, averaged over the downstream region of the storm tracks ( $60^\circ\text{W} - 30^\circ\text{E}$ ), across the ensembles (Fig. 7). Changes in the temperature field hold information on both changes in the zonal wind shear (changes in the meridional temperature gradient), and changes in static stability (changes in the vertical temperature gradient). The North Atlantic temperature response in LE (Fig. 7a) is very similar to the global warming tropospheric temperature pattern of enhanced warming in the upper tropical troposphere, relative to the upper polar troposphere, and enhanced warming in the lower polar troposphere, relative to the lower tropical troposphere (i.e., Arctic amplification). These temperature changes have opposite effects on the baroclinicity of the flow. On one hand, they act to stabilize the troposphere at low to mid-latitudes, and decrease the meridional temperature gradient at low levels, which act to reduce the baroclinicity. On the other hand, they act to destabilize the troposphere at high latitudes and increase the meridional temperature gradient aloft (**along with the vertical wind shear, Supplementary Fig. 7a**), which increases the baroclinicity (Butler et al. 2010; Yuval and Kaspi 2020).

Ocean coupling accounts for most of the tropospheric temperature changes (**and zonal wind changes, Supplementary Fig. 7b**) through all latitudes and levels (i.e., the warming of the upper tropical troposphere and Arctic amplification, Fig. 7b). This result is not surprising given that changes in surface temperature not only modify the warming of the upper tropical troposphere, by controlling the moist adiabatic lapse rate, but also modify Arctic amplification, via surface

452 feedbacks (e.g., albedo and Planck feedbacks). **Indeed, in NOM LE, the absence of ocean**  
453 **coupling processes results in only minor atmospheric warming by 2100, mostly at low-mid**  
454 **latitudes, with no significant changes to the temperature gradients (Supplementary Fig. 8a).**

455 Thermodynamic coupling (SHF, Fig. 7c) is not only responsible for the overall warming of the  
456 troposphere, but for the enhanced warming in the upper tropical troposphere, and for the Arctic  
457 amplification. **Thus, based on the growth rate analysis in Fig. 6c, thermodynamic coupling acts**  
458 **to reduce the growth rate and the TEKE response by reducing the meridional temperature**  
459 **gradient over the low-mid levels (and the associated mean zonal wind shear at mid-high**  
460 **latitudes, Supplementary Fig. 7c), and stabilizing the troposphere at low-mid latitudes. Note**  
461 **that the opposite effects of thermodynamic coupling on the meridional temperature gradient**  
462 **at low and high levels (i.e., vertical variations in the wind shear) prevents simple metrics of**  
463 **baroclinicity, which assume constant wind shear and static stability, such as the Eady growth**  
464 **rate, from capturing the effects of thermodynamic coupling on the TEKE response; the effect**  
465 **of thermodynamic coupling on the Eady growth response strongly depends on which vertical**  
466 **levels are chosen for the analysis (Supplementary Fig. 9).**

467 Dynamic coupling (OHFC, Fig. 7d), on the other hand, acts to reduce the warming of the  
468 troposphere (via the increased heat uptake **by the deep ocean**), the Arctic amplification, and  
469 the stratification of low to mid-latitudes; **in SOM LE, where OHFC changes are absent, the**  
470 **troposphere exhibits much stronger warming (due to the lack of increased ocean heat uptake**  
471 **by the deep ocean), with stronger Arctic amplification that is not confined to the surface but**  
472 **extends throughout the troposphere (Supplementary Fig. 8b).** Although dynamic coupling  
473 does not overcome the effect of thermodynamic coupling to enhance the warming of the lower  
474 Arctic troposphere, and reduce the meridional temperature gradient at low levels, it substantially  
475 reduces the effects of thermodynamic coupling to warm the mid-upper polar troposphere, which

476 results in an increase of the meridional temperature gradient aloft (**and the associated mean zonal**  
477 **wind shear at mid-high latitudes, Supplementary Fig. 7d).** As discussed above, this effect of  
478 **OHFC is due to both horizontal heat redistribution and net heat uptake by the deep ocean;**  
479 **since net heat uptake mitigates the warming of the surface, its cooling effect is also mostly**  
480 **evident over the Arctic, as it reduces the surface processes that result in Arctic amplification**  
481 **due to surface warming.** Thus, by reducing the Arctic amplification (more than the upper tropical  
482 warming), OHFC increases the meridional temperature gradient (zonal wind shear) through most  
483 of the troposphere, which increases the baroclinicity (blue bars in Fig. 6d) and thus the TEKE  
484 intensity by the end of this century.

485 **Lastly, given that ocean coupling processes affect the TEKE response via changes in SST,**  
486 **we next examine the role of ocean coupling in the future response of the surface temperature**  
487 **to anthropogenic emissions (Fig. 8).** First, the surface temperature response in LE includes  
488 **the strong warming of the Arctic, relative to lower latitudes, as well as the warming hole**  
489 **at mid-latitudes (Fig. 8a).** Second, similar to the atmospheric temperature response, ocean  
490 **coupling accounts for most of the surface temperature response (Fig. 8b); in NOM LE, the**  
491 **surface shows minor warming, even over the Arctic region (Supplementary Fig. 10a).** As a  
492 **result, in NOM LE, the melting and variability of the Arctic sea-ice are considerably reduced**  
493 **(Supplementary Fig. 11).**

494 **Decomposing the effect of ocean coupling on the surface temperature shows that thermo-**  
495 **dynamic coupling acts to warm the surface throughout the North Atlantic, but more at high**  
496 **latitudes than low latitudes, thus resulting in the Arctic amplification (Fig. 8c).** This effect  
497 **of thermodynamic coupling acts to reduce the surface (and lower troposphere) meridional**  
498 **temperature gradient (which is also evident in the SOM LE simulations, Supplementary**  
499 **Fig. 10b), and thus to reduce the growth rate and the TEKE response. Consistently, previous**

studies showed that an increase in the surface meridional temperature gradient, over the Gulf Stream region, acts to intensify the storm tracks (Brayshaw et al. 2011).

Investigating the SHF response to anthropogenic emissions (Supplementary Fig. 12) reveals that similar to the effect of thermodynamic coupling on the surface temperature, the SHF act to warm the North Atlantic SST over mid-high latitudes, and to increase oceanic heat loss to the Arctic sea-ice, which enhances the wintertime Arctic sea-ice loss and amplification (Screen and Simmonds 2010). These two processes support the thermodynamic coupling tendency to reduce the meridional temperature gradient. Further decomposing the effects of the SHF shows that sensible and latent heat fluxes are mostly responsible for the warming of the North Atlantic SST, and, together with longwave radiative fluxes, they act to enhance the oceanic heat loss (Supplementary Fig. 13).

In contrast, dynamic coupling acts to cool the surface (Fig. 8d). The overall cooling by dynamic coupling is due to the effects of net ocean heat uptake by the deep ocean; in the absence of OHFC the surface considerably warms in SOM LE, with no evidence for the North Atlantic warming hole (Chemke et al. 2020) (Supplementary Fig. 10b). The cooling by dynamic coupling is stronger at high latitudes than low latitudes, which acts to oppose the effect of thermodynamic coupling to reduce the meridional temperature gradient (Fig. 7d). As discussed above, this effect of dynamic coupling is evident throughout the polar troposphere leading to the intensification in baroclinicity and in TEKE by 2100.

### *c. The role of ocean coupling in the spread of the projected TEKE response*

The different responses of North Atlantic TEKE to anthropogenic emissions across CMIP5 models (gray bars in Fig. 3b) could arise from both the different models' formulations, and from the internal climate variability. In LE, on the other hand, the different TEKE responses across

the LE members only stem from the internal climate variability. While the LE mean shows a similar intensification of the TEKE to the CMIP5 mean intensification (compare red and black lines in Fig. 3b), **the spread across the LE members ( $3.9 \times 10^9 \text{ J}^2 \text{ m}^{-4}$ , defined as the variance of the TEKE response across the LE members, Fig. 6a) is approximately a quarter of the spread across CMIP5 models ( $1.6 \times 10^{10} \text{ J}^2 \text{ m}^{-4}$ , Fig. 3b). Thus, assuming that the spread of the TEKE response across the LE members is similar in other ensembles of CMIP5 models (and that the ensemble members are independent of the different models' formulations, i.e., their covariance is zero),  $\sim 25\%$  of the spread in the TEKE response across CMIP5 models is due to internal variability, while the other  $\sim 75\%$  is due to the different formulations of CMIP5 models.**

Given the important role of ocean coupling in the forced response of the TEKE to anthropogenic emission, we next assess the effect of ocean coupling on the spread of the TEKE response in LE. **The spread in the TEKE response in NOM LE (i.e., with no ocean coupling) of  $4.9 \times 10^9 \text{ J}^2 \text{ m}^{-4}$  captures all of the spread across the LE members (compare red and gray bars in Fig. 6a). Thus, while ocean coupling has an important role in the forced response of the TEKE to anthropogenic emissions, it has a minor effect on the spread of the TEKE response in LE (i.e., on their internal variability). Interestingly, the LE was found to underestimate part of the multidecadal variability in North Atlantic oceanic processes (Kim et al. 2018). Thus, while it is conceivable that the internal variability, estimated from the LE, should have explained a larger portion of the CMIP5 spread, the minor effect of ocean coupling on the internal variability in LE suggests that the multidecadal ocean variability biases in LE are less likely to affect the above result.**

As discussed in Sec. 1, Woollings et al. (2012) suggested, using correlation analysis, that the different weakening of AMOC across CMIP3 models might explain half of the spread in the storm

tracks response across the models. Here, on the other hand, since the ocean has a relatively minor effect on the spread across the LE members, the weakening of AMOC (defined, following Woollings et al. 2012, as the maximum value of the wintertime Atlantic meridional streamfunction at  $45^\circ$ ) and the TEKE response are poorly correlated across the ensemble members, with  $r = -0.07$  (Fig. 9). **We suggest that any previously suggested effects that AMOC weakening may have on the spread of the storm tracks' response across different models is not likely due to internal variability, but due to the different models' formulations.**

#### 4. Summary

Previous studies have argued for the importance of ocean-atmosphere coupling, and in particular of dynamic coupling (OHFC changes), in the projected response of North Atlantic storm tracks to anthropogenic emissions. However, to date, the roles of ocean coupling and its different components in modifying the storm tracks' response **are not fully understood**. Using the **CESM1** we construct a hierarchy of ocean coupling experiments (including fully-coupled, fixed OHFC and fixed SST configurations) in large ensembles of model simulations forced across the 20th and 21st centuries under the Historical and RCP8.5 forcings. Such a hierarchy not only allows us to isolate and quantify the role of ocean coupling in the North Atlantic TEKE response, but also to further decompose the role of ocean coupling to thermodynamic ocean coupling (the effects of surface heat fluxes) and dynamic coupling (the effects of OHFC). We find that by the end of this century ocean coupling accounts for nearly all of the strengthening of North Atlantic TEKE over the downstream region of the storm tracks. While surface heat fluxes act to weaken the TEKE by the end of this century, OHFC changes overcome this weakening effect, and are found to be responsible for the intensification of North Atlantic TEKE. Further decomposing the role of OHFC changes reveals that horizontal heat redistribution by ocean heat transport **and non uniform heat uptake** accounts

for two thirds of the effect of OHFC to intensify the TEKE, while one third is due to the effect of net oceanic heat uptake **by the deep ocean** to delay surface warming.

Investigating the mechanism underlying the effect of ocean coupling on North Atlantic TEKE reveals that ocean coupling **intensifies** the TEKE by modulating the zonal wind shear. In particular, OHFC changes increase the meridional temperature gradient (i.e., zonal wind shear) in the middle-to-upper troposphere, by reducing the Arctic amplification (i.e., the larger warming of the Arctic relative to lower latitudes), which increases the growth rate of North Atlantic eddies, and intensifies the TEKE. In addition, we show that while ocean coupling are responsible for the forced intensification of North Atlantic TEKE, it has a relatively minor effect on the internal variability (inter-member spread) of the TEKE response. **Thus, any previously suggested role of AMOC weakening in explaining the spread in the storm tracks' response across the models is not likely due to internal variability, but might solely stem from the effect of the different models' formulations on the AMOC response (Todd et al. 2020).**

Finally, given that the strengthening of North Atlantic TEKE is found to arise from OHFC changes, it is important to elucidate which OHFC processes are responsible for intensifying the TEKE. While the answer to this question is beyond the scope of this manuscript, the low correlation between the intensification of the TEKE and the weakening of AMOC across the LE members suggests that the wind-driven circulation might play an important role in the intensification of the TEKE (Woollings et al. 2012).

*Acknowledgments.* We are grateful to Ivan Mitevski for analyzing the GISS ModelE data. R.C. is supported by the Israeli Science Foundation Grant 906/21.

*Data availability statement.* The data used in the manuscript is publicly available for CMIP5 at <https://esgf-node.llnl.gov/projects/cmip5/>, and for the CESM LE at

593 [http : //www.cesm.ucar.edu/](http://www.cesm.ucar.edu/). Data from SOM LE and NOM LE is available upon request from:  
594 rei.chemke@weizmann.ac.il. The GISS and GFDL simulations are available upon request from  
595 clara.orbe@nasa.gov and lori.sentman@noaa.gov, respectively.

## 596 References

- 597 Bellomo, K., M. Angeloni, S. Corti, and J. von Hardenberg, 2021: Future climate change shaped by  
598 inter-model differences in Atlantic meridional overturning circulation response. *Nat. Commun.*,  
599 **12**, 3659.
- 600 Bitz, C. M., K. M. Shell, P. R. Gent, D. A. Bailey, G. Danabasoglu, K. C. Armour, M. M. Holland,  
601 and J. T. Kiehl, 2012: Climate Sensitivity of the Community Climate System Model, Version 4.  
602 *J. Clim.*, **25**, 3053–3070.
- 603 Brayshaw, D. J., B. Hoskins, and M. Blackburn, 2011: The basic ingredients of the North Atlantic  
604 storm track. Part II: Sea surface temperatures. *J. Atmos. Sci.*, **68**, 1784–1805.
- 605 Butler, A. H., D. W. J. Thompson, and R. Heikes, 2010: The Steady-State Atmospheric Circulation  
606 Response to Climate Change-like Thermal Forcings in a Simple General Circulation Model. *J.*  
607 *Clim.*, **23**, 3474–3496.
- 608 Ceppi, P., G. Zappa, T. G. Shepherd, and J. M. Gregory, 2018: Fast and Slow Components of the  
609 Extratropical Atmospheric Circulation Response to CO<sub>2</sub> Forcing. *J. Clim.*, **31**, 1091–1105.
- 610 Chang, E. K. M., Y. Guo, and X. Xia, 2012: CMIP5 multimodel ensemble projection of storm  
611 track change under global warming. *J. Geophys. Res.*, **117** (D16), D23118.
- 612 Chemke, R., and Y. Ming, 2020: Large atmospheric waves will get stronger, while small waves  
613 will get weaker by the end of the 21st century. *Geophys. Res. Lett.*, **47** (22), e2020GL090441.

614 Chemke, R., and L. M. Polvani, 2018: Ocean circulation reduces the Hadley cell response to  
615 increased greenhouse gases. *Geophys. Res. Lett.*, **45**, 9197–9205.

616 Chemke, R., and L. M. Polvani, 2019: Exploiting the abrupt 4xco2 scenario to elucidate tropical  
617 expansion mechanisms. *J. Clim.*, **32** (3), 859–875.

618 Chemke, R., L. M. Polvani, and C. Deser, 2019: The Effect of Arctic Sea Ice Loss on the Hadley  
619 Circulation. *Geophys. Res. Lett.*, **46** (2), 963–972.

620 Chemke, R., L. Zanna, and L. M. Polvani, 2020: Identifying a human signal in the North Atlantic  
621 warming hole. *Nat. Commun.*, **11**, 1540.

622 Ciasto, L. M., C. Li, J. J. Wettstein, and N. G. Kvamstø, 2016: North Atlantic Storm-Track  
623 Sensitivity to Projected Sea Surface Temperature: Local versus Remote Influences. *J. Clim.*,  
624 **29** (19), 6973–6991.

625 Coumou, D., J. Lehmann, and J. Beckmann, 2015: The weakening summer circulation in the  
626 Northern Hemisphere mid-latitudes. *Science*, **348** (6232), 324–327.

627 Czaja, A., C. Frankignoul, S. Minobe, and B. Vanniere, 2019: Simulating the Midlatitude At-  
628 mospheric Circulation: What Might We Gain From High-Resolution Modeling of Air-Sea  
629 Interactions? *Curr. Clim. Change Rep.*, **5**, 390–406.

630 Deser, C., L. Sun, R. A. Tomas, and J. Screen, 2016: Does ocean coupling matter for the northern  
631 extratropical response to projected Arctic sea ice loss? *Geophys. Res. Lett.*, **43**, 2149–2157.

632 Frankignoul, C., G. Gastineau, and Y. Kwon, 2013: The Influence of the AMOC Variability on the  
633 Atmosphere in CCSM3. *J. Clim.*, **26** (24), 9774–9790.

634 Gastineau, G., F. D’Andrea, and C. Frankignoul, 2013: Atmospheric response to the North Atlantic  
635 Ocean variability on seasonal to decadal time scales. *Clim. Dyn.*, **40** (9-10), 2311–2330.

636 Gervais, M., J. Shaman, and Y. Kushnir, 2019: Impacts of the North Atlantic Warming Hole in  
637 Future Climate Projections: Mean Atmospheric Circulation and the North Atlantic Jet. *J. Clim.*,  
638 **32 (10)**, 2673–2689.

639 Grise, K. M., and L. M. Polvani, 2017: Understanding the Time Scales of the Tropospheric  
640 Circulation Response to Abrupt CO<sub>2</sub> Forcing in the Southern Hemisphere: Seasonality and the  
641 Role of the Stratosphere. *J. Clim.*, **30**, 8497–8515.

642 Harvey, B. J., P. Cook, L. C. Shaffrey, and R. Schiemann, 2020: The Response of the Northern  
643 Hemisphere Storm Tracks and Jet Streams to Climate Change in the CMIP3, CMIP5, and CMIP6  
644 Climate Models. *J. Geophys. Res.*, **125 (23)**, e32701.

645 Harvey, B. J., L. C. Shaffrey, and T. J. Woollings, 2014: Equator-to-pole temperature differences  
646 and the extra-tropical storm track responses of the CMIP5 climate models. *Clim. Dyn.*, **43 (5-6)**,  
647 1171–1182.

648 Held, I. M., H. Guo, A. Adcroft, J. P. Dunne, L. W. Horowitz, and J. Krasting et al., 2019: Structure  
649 and performance of GFDL’s CM4.0 climate model. *J. Adv. Mod. Earth Syst.*, **11**, 3691–3727.

650 Hurrell, J. W., and Coauthors, 2013: The Community Earth System Model: A Framework for  
651 Collaborative Research. *Bull. Am. Meteor. Soc.*, **94**, 1339–1360.

652 Kay, J. E., and Coauthors, 2015: The Community Earth System Model (CESM) Large Ensemble  
653 Project: A Community Resource for Studying Climate Change in the Presence of Internal  
654 Climate Variability. *Bull. Am. Meteor. Soc.*, **96**, 1333–1349.

655 Kelley, M., G. A. Schmidt, L. Nazarenko, R. L. Miller, S. E. Bauer, R. Ruedy, and G. L.  
656 Russell et al., 2020: GISS-E2.1: Configurations and climatology. *J. Adv. Mod. Earth Syst.*, **12**,  
657 e2019MS002025.

Kim, W. M., S. Yeager, P. Chang, and G. Danabasoglu, 2018: Low-Frequency North Atlantic Climate Variability in the Community Earth System Model Large Ensemble. *J. Clim.*, **31**, 787–813.

Lehmann, J., D. Coumou, K. Frieler, A. V. Eliseev, and A. Levermann, 2014: Future changes in extratropical storm tracks and baroclinicity under climate change. *Env. Res. Lett.*, **9** (8), 084002.

Magnusdottir, G., C. Deser, and R. Saravanan, 2004: The Effects of North Atlantic SST and Sea Ice Anomalies on the Winter Circulation in CCM3. Part I: Main Features and Storm Track Characteristics of the Response. *J. Clim.*, **17** (5), 857–876.

O’Gorman, P. A., and T. Schneider, 2008: Energy in midlatitude transient eddies in idealized simulations of changed climates. *J. Clim.*, **21**, 5797–5806.

Riahi, K., and Coauthors, 2011: RCP 8.5 - A scenario of comparatively high greenhouse gas emissions. *Clim. Change*, **109** (1-2), 33–57.

Screen, J. A., and I. Simmonds, 2010: Increasing fall-winter energy loss from the Arctic Ocean and its role in Arctic temperature amplification. *Geophys. Res. Lett.*, **37** (16), L16707.

Smith, K. S., 2007: The geography of linear baroclinic instability in earth’s oceans. *J. Mar. Res.*, **65** (5), 655–683.

Taylor, K. E., R. J. Stouffer, and G. A. Meehl, 2012: An Overview of CMIP5 and the Experiment Design. *Bull. Am. Meteor. Soc.*, **93**, 485–498.

Todd, A., and Coauthors, 2020: Ocean-Only FAFMIP: Understanding Regional Patterns of Ocean Heat Content and Dynamic Sea Level Change. *J. Adv. Mod. Earth Syst.*, **12** (8), e02027.

- 678 Woollings, T., J. M. Gregory, J. G. Pinto, M. Meyers, and D. J. Brayshaw, 2012: Response of  
679 the North Atlantic storm track to climate change shaped by ocean-atmosphere coupling. *Nat.*  
680 *Geosci.*, **5**, 313–317.
- 681 Yuval, J., and Y. Kaspi, 2020: Eddy activity response to global warming-like temperature changes.  
682 *J. Clim.*, **33** (4), 1381–1404.
- 683 Zappa, G., L. C. Shaffrey, K. I. Hodges, P. G. Sansom, and D. B. Stephenson, 2013: A Multimodel  
684 Assessment of Future Projections of North Atlantic and European Extratropical Cyclones in the  
685 CMIP5 Climate Models. *J. Clim.*, **26** (16), 5846–5862.

## LIST OF FIGURES

- Fig. 1.** Preindustrial climatology of DJF TEKE in the fully coupled (left) and slab ocean (right) models of the CESM1. . . . . 35
- Fig. 2.** One standard deviation of DJF North Atlantic TEKE, over the downstream region of the storm tracks, across different number of ensemble members. The standard deviation is calculated each year, and averaged over the 1920-2100 period, and over all combinations of number of ensemble members (or up to 1000 random combinations) in LE (red), SOM LE (blue) and NOM LE (green). Error bars show the standard deviation across the different combinations of number of ensemble members. **Vertical lines show the number of members that capture 99% of the TEKE variability across all members.** . . . . . 36
- Fig. 3.** (a) The response to anthropogenic emissions (difference between the last 20 years of the 21st and 20th centuries) of DJF North Atlantic TEKE ( $\text{Jm}^{-2}$ ) in CMIP5 mean (shading). Black contours show the TEKE averaged over the last 20 years of the 20th century in intervals of  $3 \times 10^5 \text{Jm}^{-2}$ , with a maximum value of  $2.2 \times 10^6 \text{Jm}^{-2}$ . Black dots show where the response is statistically insignificant at the 95% confidence level based on a Student's t-test at every 5th grid point, for plotting purposes. Green box shows the downstream region of the storm tracks. (b) The occurrence frequency of the TEKE response ( $10^5 \text{Jm}^{-2}$ ) averaged over the downstream region of the storm tracks in CMIP5 models (gray bars). Vertical black and red lines show the CMIP5 mean and LE mean, respectively. One standard deviation across the LE members is  $6.2 \times 10^4 \text{Jm}^{-2}$ . . . . . 37
- Fig. 4.** (a) The response to anthropogenic emissions of DJF North Atlantic TEKE ( $\text{Jm}^{-2}$ ) in LE mean (shading). Black contours show the TEKE averaged over the last 20 years of the 20th century in intervals of  $5 \times 10^5 \text{Jm}^{-2}$ , with a maximum value of  $3 \times 10^6 \text{Jm}^{-2}$ . Green box shows the downstream region of the storm tracks. The relative contribution to the response of the TEKE in LE from (b) ocean coupling (difference between LE and NOM LE), and from decomposing the ocean coupling to (c) thermodynamic coupling (surface heat fluxes, SHF; difference between SOM LE and NOM LE) and (d) dynamic coupling (ocean heat flux convergence, OHFC; difference between LE and SOM LE). Black dots show where the response is statistically insignificant at the 95% confidence level based on a Student's t-test. . . . . 38
- Fig. 5.** The response to quadrupling of  $\text{CO}_2$  concentrations, relative to preindustrial values, of DJF North Atlantic TEKE ( $\text{Jm}^{-2}$ , shading) in (a) GISS Model E2.1, and (c) GFDL CM4. Black contours show the TEKE preindustrial climatology in intervals of  $5 \times 10^5 \text{Jm}^{-2}$ , with a maximum value of  $3 \times 10^6 \text{Jm}^{-2}$  in panel a and of  $2.5 \times 10^6 \text{Jm}^{-2}$  in panel c. The relative contribution to the response of the TEKE from dynamic coupling (OHFC) in (b) GISS Model E2.1 and (d) GFDL CM4. . . . . 39
- Fig. 6.** (a) The occurrence frequency of DJF North Atlantic TEKE response to anthropogenic emissions ( $10^5 \text{Jm}^{-2}$ ) averaged over the downstream region of the storm tracks in LE (red bars). The relative contribution to the TEKE response from ocean coupling (gray bars), and from decomposing the ocean coupling to thermodynamic coupling (SHF, green bars) and dynamic coupling (OHFC, blue bars). Vertical red, dashed black, green and blue lines show the LE mean response, mean ocean contribution, mean SHF contribution and mean OHFC contribution, respectively. (b) The occurrence frequency of TEKE response normalized by the global mean SST response ( $10^4 \text{Jm}^{-2}\text{K}^{-1}$ ) in LE (red bars), and the relative contribution from dynamic coupling (OHFC, blue bars). Vertical red and blue lines show the LE mean response and mean OHFC contribution, respectively. (c) The growth rate response ( $10^{-6} \text{s}^{-1}$ ) in LE mean (red bar), and the relative contribution to the response of the growth rate from ocean coupling (gray bar), and from decomposing the ocean coupling to thermodynamic

733	coupling (SHF, green bar) and dynamic coupling (OHFC, blue bar). (d) The relative con-	
734	tribution to the growth rate response from the mean zonal wind ( $u$ ), static stability ( $S^2$ ) and	
735	tropopause height ( $p_{\text{trop}}$ ) in LE (red bars), the contributions from ocean coupling (gray bars),	
736	thermodynamic coupling (SHF, green bars) and dynamic coupling (OHFC, blue bars). The	
737	error bars show the 95% confidence interval based on a Student's t-distribution. . . . .	40
738	<b>Fig. 7.</b> As in Fig. 4 only for the mean temperature averaged over the downstream region of the storm	
739	tracks ( $60^\circ\text{W} - 30^\circ\text{E}$ ). . . . .	41
740	<b>Fig. 8.</b> As in Fig. 4 only for the surface temperature response (K). . . . .	42
741	<b>Fig. 9.</b> The response to anthropogenic emissions of DJF North Atlantic TEKE ( $10^5 \text{ Jm}^{-2}$ ) averaged	
742	over the downstream region of the storm tracks as a function of the AMOC response (Sv) in	
743	LE. Their correlation appears in the upper left corner. . . . .	43

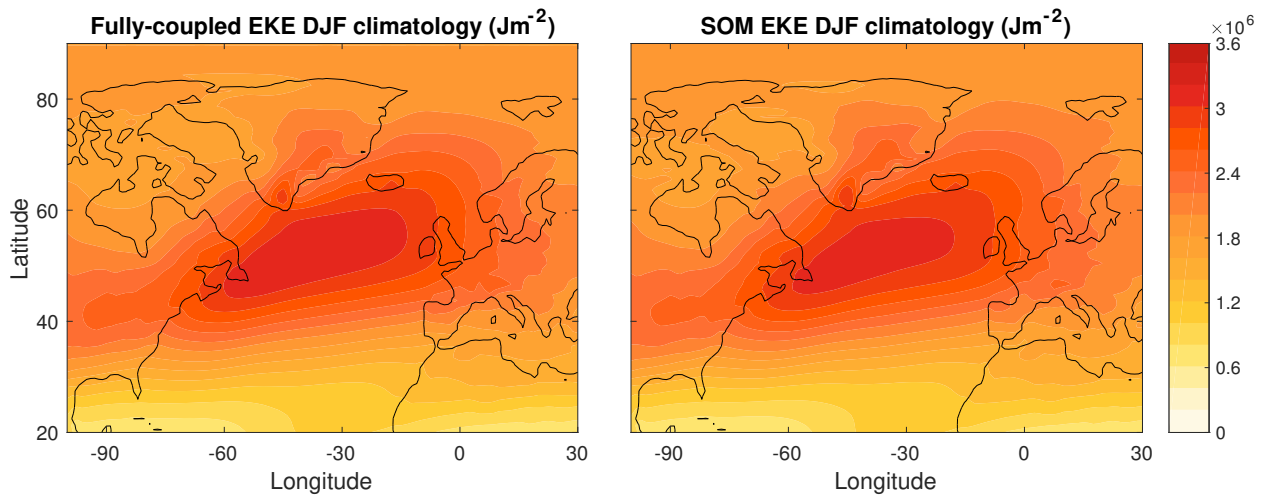


FIG. 1. Preindustrial climatology of DJF TEKE in the fully coupled (left) and slab ocean (right) models of the CESM1.

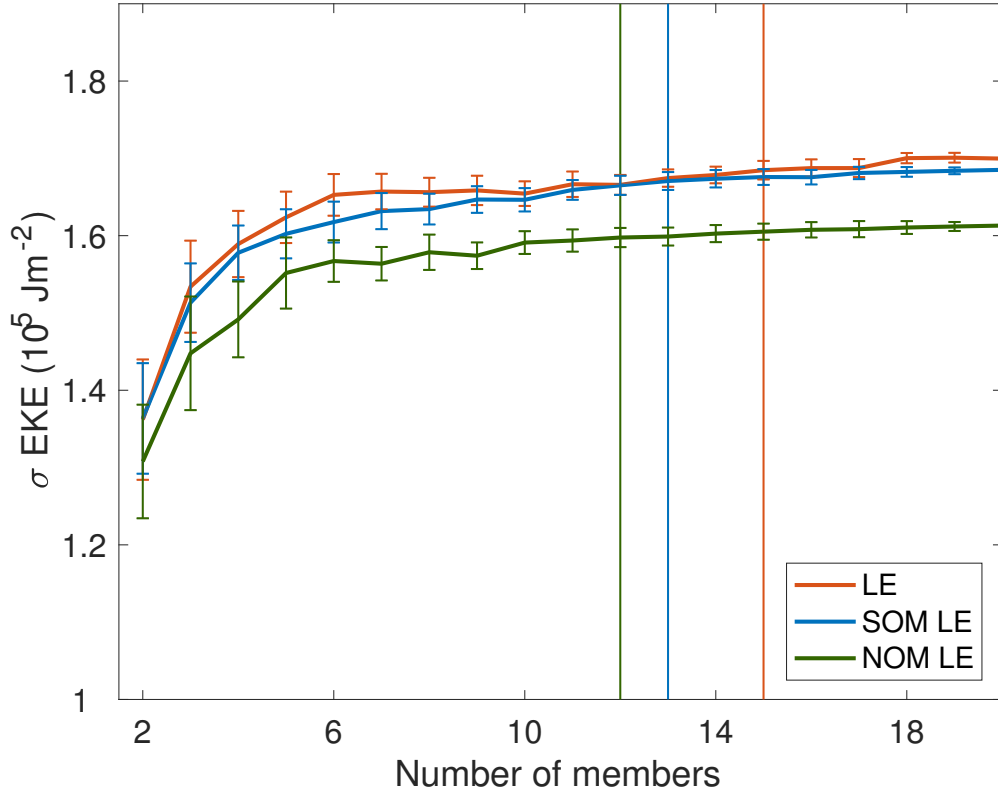


FIG. 2. One standard deviation of DJF North Atlantic TEKE, over the downstream region of the storm tracks, across different number of ensemble members. The standard deviation is calculated each year, and averaged over the 1920-2100 period, and over all combinations of number of ensemble members (or up to 1000 random combinations) in LE (red), SOM LE (blue) and NOM LE (green). Error bars show the standard deviation across the different combinations of number of ensemble members. **Vertical lines show the number of members that capture 99% of the TEKE variability across all members.**

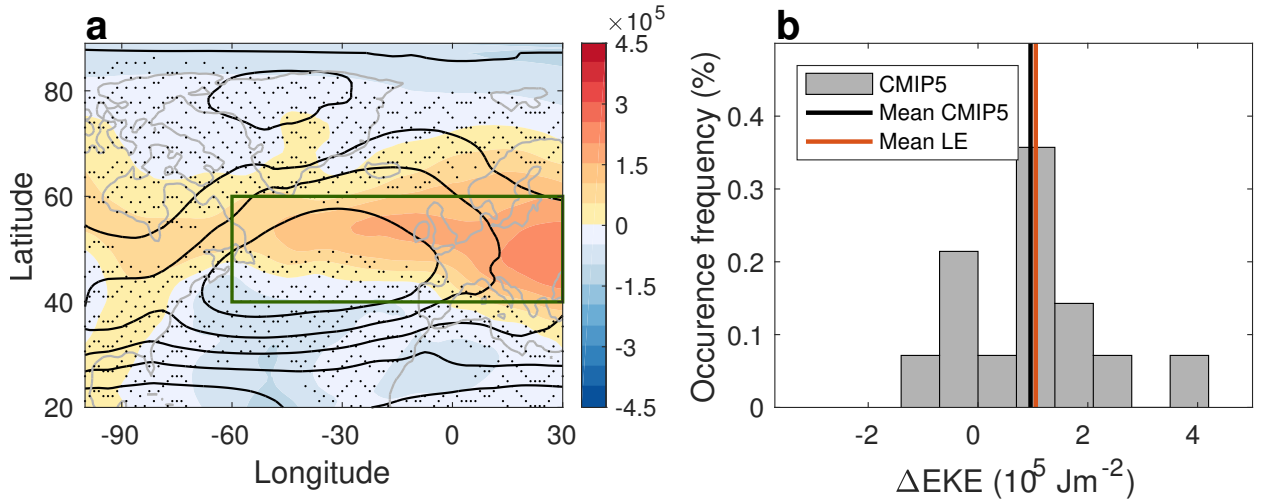


FIG. 3. (a) The response to anthropogenic emissions (difference between the last 20 years of the 21st and 20th centuries) of DJF North Atlantic TEKE ( $\text{Jm}^{-2}$ ) in CMIP5 mean (shading). Black contours show the TEKE averaged over the last 20 years of the 20th century in intervals of  $3 \times 10^5 \text{ Jm}^{-2}$ , with a maximum value of  $2.2 \times 10^6 \text{ Jm}^{-2}$ . Black dots show where the response is statistically insignificant at the 95% confidence level based on a Student's t-test at every 5th grid point, for plotting purposes. Green box shows the downstream region of the storm tracks. (b) The occurrence frequency of the TEKE response ( $10^5 \text{ Jm}^{-2}$ ) averaged over the downstream region of the storm tracks in CMIP5 models (gray bars). Vertical black and red lines show the CMIP5 mean and LE mean, respectively. One standard deviation across the LE members is  $6.2 \times 10^4 \text{ Jm}^{-2}$ .

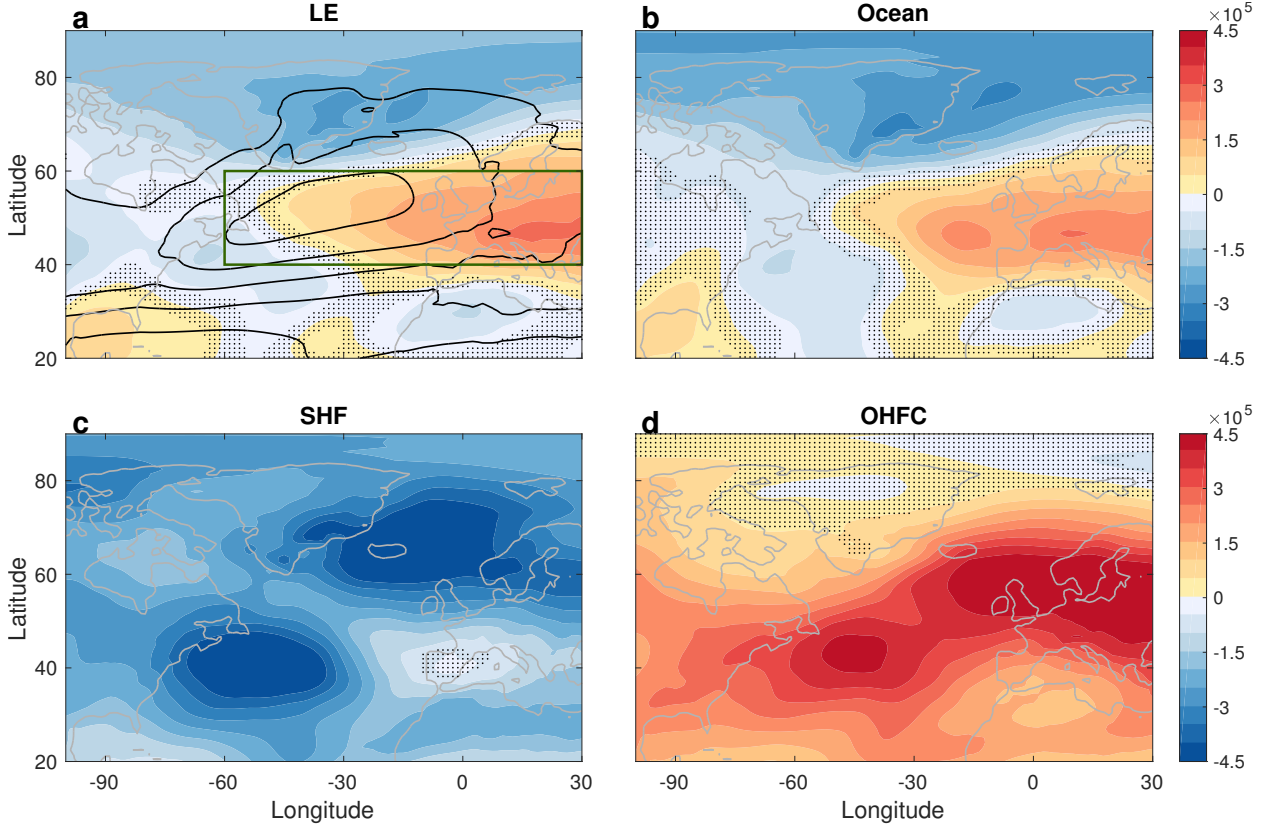


FIG. 4. (a) The response to anthropogenic emissions of DJF North Atlantic TEKE ( $\text{Jm}^{-2}$ ) in LE mean (shading). Black contours show the TEKE averaged over the last 20 years of the 20th century in intervals of  $5 \times 10^5$   $\text{Jm}^{-2}$ , with a maximum value of  $3 \times 10^6$   $\text{Jm}^{-2}$ . Green box shows the downstream region of the storm tracks. The relative contribution to the response of the TEKE in LE from (b) ocean coupling (difference between LE and NOM LE), and from decomposing the ocean coupling to (c) thermodynamic coupling (surface heat fluxes, SHF; difference between SOM LE and NOM LE) and (d) dynamic coupling (ocean heat flux convergence, OHFC; difference between LE and SOM LE). Black dots show where the response is statistically insignificant at the 95% confidence level based on a Student's t-test.

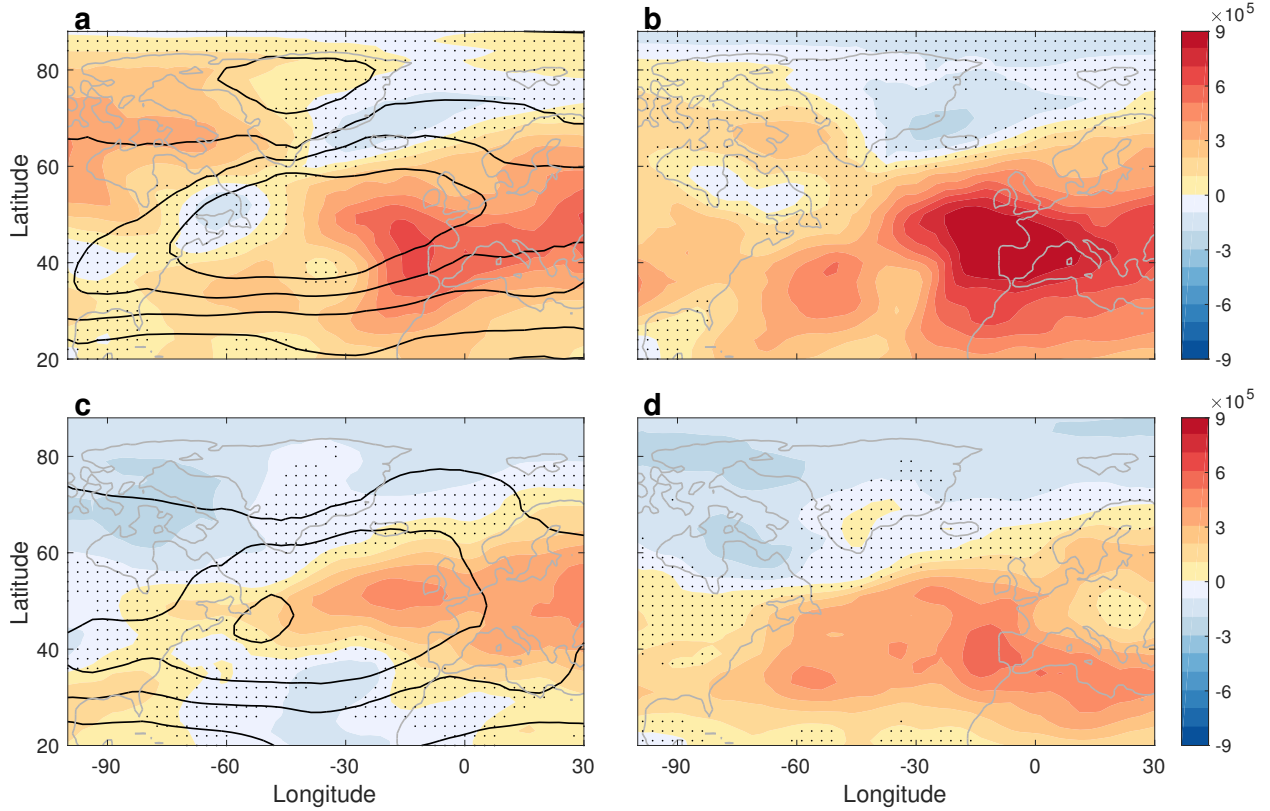


FIG. 5. The response to quadrupling of CO<sub>2</sub> concentrations, relative to preindustrial values, of DJF North Atlantic TEKE (Jm<sup>-2</sup>, shading) in (a) GISS Model E2.1, and (c) GFDL CM4. Black contours show the TEKE preindustrial climatology in intervals of  $5 \times 10^5 \text{ Jm}^{-2}$ , with a maximum value of  $3 \times 10^6 \text{ Jm}^{-2}$  in panel a and of  $2.5 \times 10^6 \text{ Jm}^{-2}$  in panel c. The relative contribution to the response of the TEKE from dynamic coupling (OHFC) in (b) GISS Model E2.1 and (d) GFDL CM4.

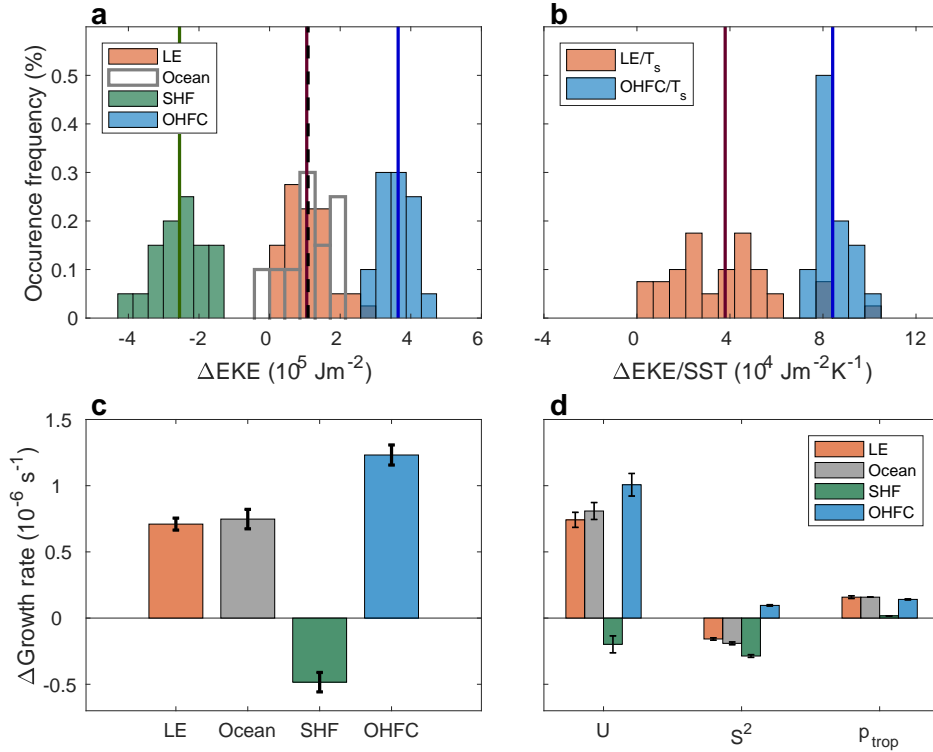


FIG. 6. (a) The occurrence frequency of DJF North Atlantic TEKE response to anthropogenic emissions ( $10^5 \text{ Jm}^{-2}$ ) averaged over the downstream region of the storm tracks in LE (red bars). The relative contribution to the TEKE response from ocean coupling (gray bars), and from decomposing the ocean coupling to thermodynamic coupling (SHF, green bars) and dynamic coupling (OHFC, blue bars). Vertical red, dashed black, green and blue lines show the LE mean response, mean ocean contribution, mean SHF contribution and mean OHFC contribution, respectively. (b) The occurrence frequency of TEKE response normalized by the global mean SST response ( $10^4 \text{ Jm}^{-2}\text{K}^{-1}$ ) in LE (red bars), and the relative contribution from dynamic coupling (OHFC, blue bars). Vertical red and blue lines show the LE mean response and mean OHFC contribution, respectively. (c) The growth rate response ( $10^{-6} \text{ s}^{-1}$ ) in LE mean (red bar), and the relative contribution to the response of the growth rate from ocean coupling (gray bar), and from decomposing the ocean coupling to thermodynamic coupling (SHF, green bar) and dynamic coupling (OHFC, blue bar). (d) The relative contribution to the growth rate response from the mean zonal wind ( $u$ ), static stability ( $S^2$ ) and tropopause height ( $p_{\text{trop}}$ ) in LE (red bars), the contributions from ocean coupling (gray bars), thermodynamic coupling (SHF, green bars) and dynamic coupling (OHFC, blue bars). The error bars show the 95% confidence interval based on a Student's t-distribution.

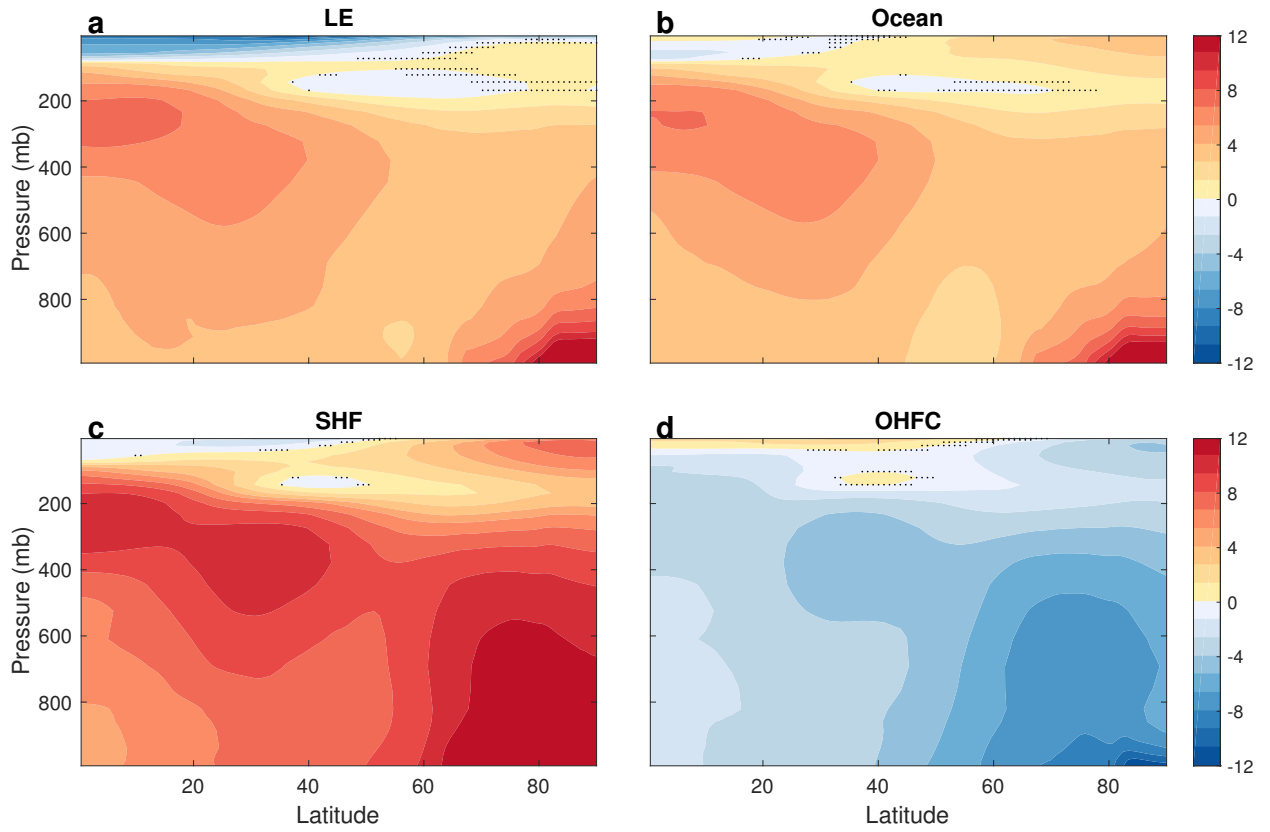


FIG. 7. As in Fig. 4 only for the mean temperature averaged over the downstream region of the storm tracks (60°W – 30°E).

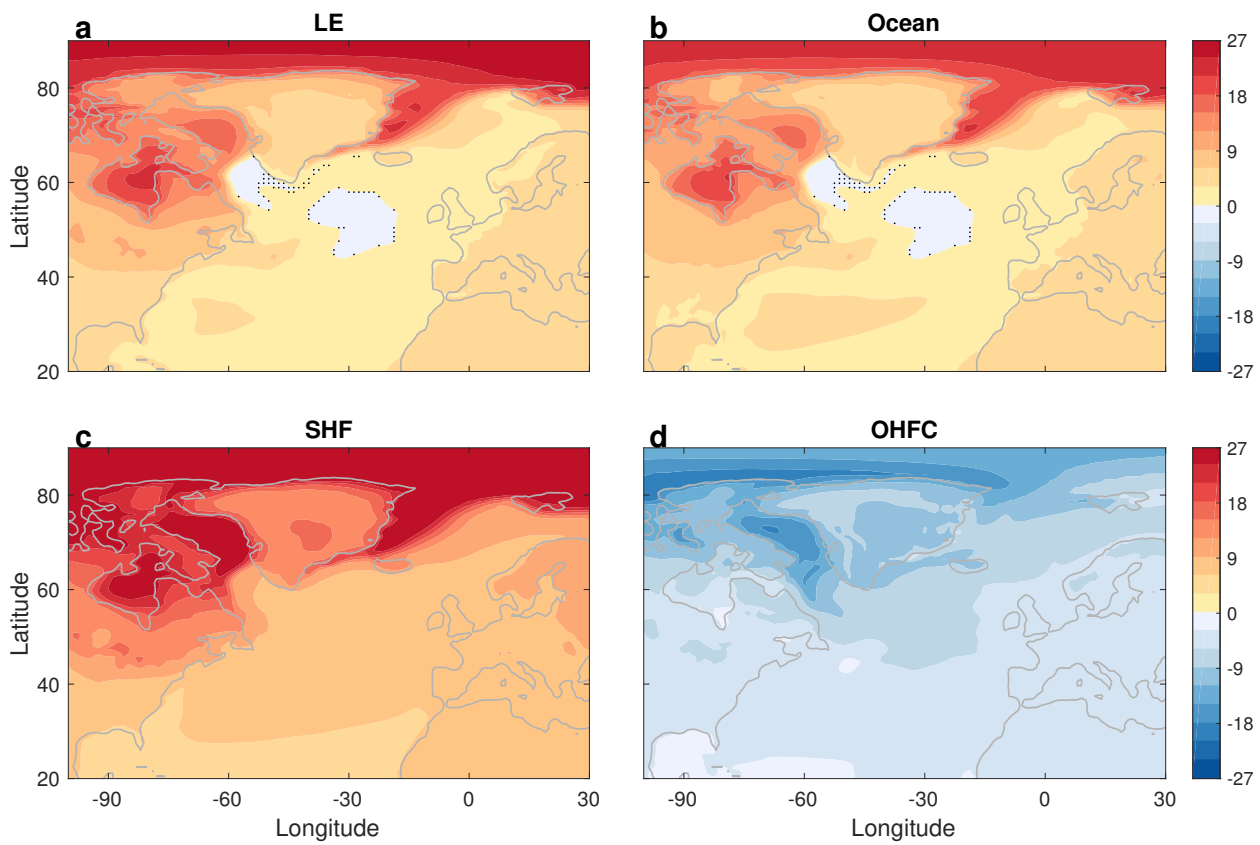


FIG. 8. As in Fig. 4 only for the surface temperature response (K).

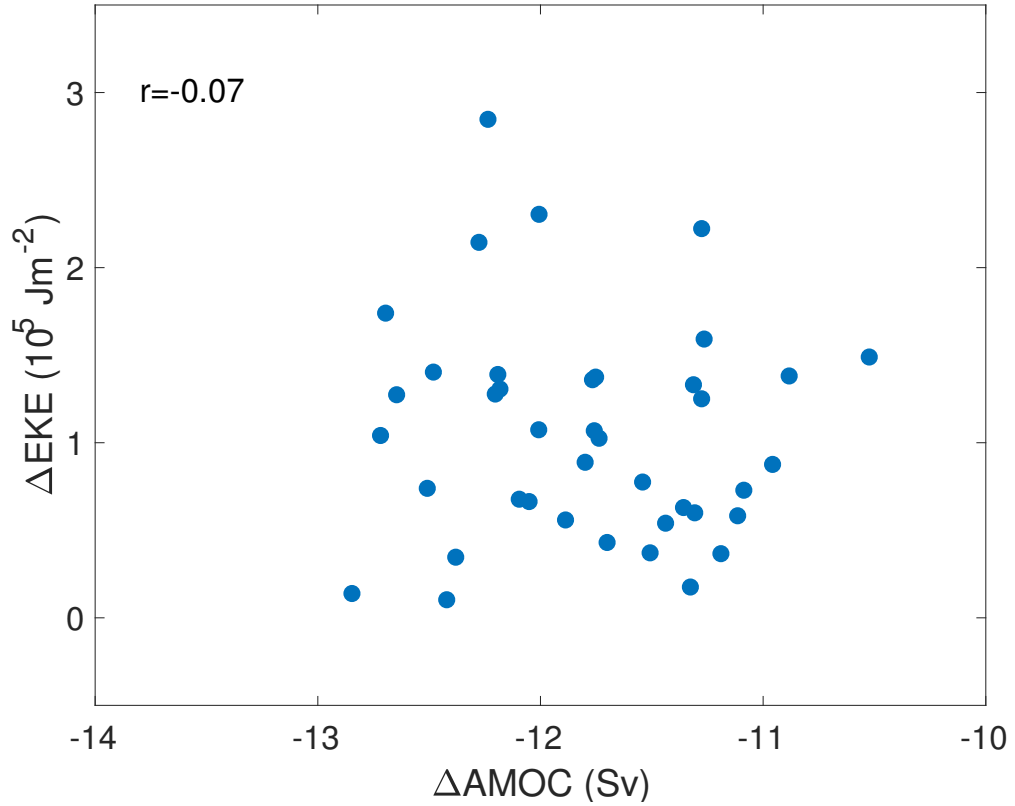


FIG. 9. The response to anthropogenic emissions of DJF North Atlantic TEKE ( $10^5 \text{ Jm}^{-2}$ ) averaged over the downstream region of the storm tracks as a function of the AMOC response (Sv) in LE. Their correlation appears in the upper left corner.